

# The Impact of Gradient Wind Imbalance on Potential Intensity of Tropical Cyclones in an Unbalanced Slab Boundary Layer Model

THOMAS FRISIUS AND DARIA SCHÖNEMANN

*CliSAP Research Group Dynamical Systems, KlimaCampus, University of Hamburg, Hamburg, Germany*

JONATHAN VIGH

*Research Applications Laboratory, NCAR,\* Boulder, Colorado*

(Manuscript received 8 June 2012, in final form 18 February 2013)

## ABSTRACT

The assumption of gradient wind balance is customarily made so as to derive the theoretical upper-bound intensity of a mature tropical cyclone. Emanuel's theory of hurricane potential intensity (E-PI) makes use of this assumption, whereas more recent studies by Bryan and Rotunno demonstrate that the effect of unbalanced flow can result in maximum winds that are well in excess of E-PI (superintensity). The existence of supergradient winds has been verified in a slab boundary layer model developed by Smith. Here, the authors apply the slab boundary layer model within the framework of classical E-PI theory to investigate the sensitivity of supergradient winds to the radius of maximum gradient wind (RMGW) and four nondimensional model parameters. The authors find that the Rossby number, the drag coefficient, and the modified Rankine decay parameter all have a considerable influence on the strength of the unbalanced flow. In contrast, the ratio of surface exchange coefficients has little noticeable effect on superintensity. The inclusion of horizontal momentum diffusion leads to a weaker superintensity, but the qualitative features of the model remain similar. To further elucidate these findings, the authors use the boundary layer model to examine the modified E-PI theory proposed by Emanuel and Rotunno. They assume a constant Richardson number for the outflow. The boundary layer model driven by the modified E-PI solution depends on just three model parameters rather than the four parameters used in the classical E-PI framework. Despite this apparent advantage, the results obtained in the framework of the modified E-PI are less realistic than those computed with the classical E-PI approach.

## 1. Introduction

Bryan and Rotunno (2009, hereafter BR09) recently demonstrated that gradient wind imbalance can explain a substantial increase of intensity in a numerically simulated axisymmetric tropical cyclone (TC). (Throughout this paper, intensity is defined to be the maximum tangential wind speed found in the boundary layer of the TC.) Therefore, gradient wind imbalance probably explains a large portion of superintensity, defined as the

excess of the wind speed over the potential intensity (PI) predicted by the classical potential intensity theory of Emanuel (1986, hereafter referred to as E-PI). Besides gradient wind imbalance, the presence of nonzero convective available potential energy (CAPE) can also contribute to superintensity. While the current paper focuses on the role of gradient wind imbalance, the influence of CAPE on superintensity has recently been evaluated by the authors in an extended PI model (Frisius and Schönemann 2012).

Superintensity has been found in a number of numerical high-resolution simulations of TCs including Persing and Montgomery (2003), Hausman et al. (2006), BR09, Frisius and Schönemann (2012), and Wang and Xu (2010). BR09 also derived an analytical model that includes gradient wind imbalance. While their analytical model is in excellent agreement with their numerical model, it cannot be used a priori for the prediction of

---

\*The National Center for Atmospheric Research is sponsored by the National Science Foundation.

---

*Corresponding author address:* Thomas Frisius, CRG Dynamical Systems, KlimaCampus, Universität Hamburg, Grindelberg 5, D-20144 Hamburg, Germany.  
E-mail: thomas.frisius@zmaw.de

supergradient winds. This is because the analytical model depends upon parameters that have to be evaluated by the numerical model itself [see Eq. (23) of BR09].

In this study, we devise a method to evaluate superintensity within the classical PI model of Emanuel (1986, hereafter E86) this method includes the effect of supergradient winds. For this purpose, we base our calculations on the unbalanced slab boundary model of Smith (2003), where all properties are assumed to be vertically independent within the boundary layer. The existence of supergradient winds in this model has already been demonstrated by Smith et al. (2008), who prescribed the gradient wind as in the E-PI model. Here, we apply the slab boundary layer model over a wide range of relevant parameters so as to delineate the supergradient wind regime. Additionally, the model predicts the overshoot of inflow beyond the radius of maximum gradient wind (RMGW) and the mass flux into the eyewall. The results are found to depend strongly on the horizontal scale of the TC. Therefore, the present model exhibits a scale dependence that is not found in the classical PI model.

We are aware of the criticisms of slab boundary layer models by Kepert (2010a,b). In those studies, it was shown in a diagnostic height-resolving model that slab boundary layer models overestimate the radial inflow and, therefore, deliver too strong supergradient winds. This is due to the inaccurate calculation of surface drag as a function of the vertically averaged boundary layer wind. On the other hand, a correction of the drag, by simply reducing the surface drag coefficient, leads to an early breakdown of the inflow outside the radius of maximum gradient wind. Kepert demonstrates that the latter tendency is a result of the false evaluation of radial advection in the slab boundary layer model. Nevertheless, we think that the slab boundary layer offers at least a qualitatively valid representation of the appearance and organization of supergradient winds in a tropical cyclone.

This study is structured as follows. Section 2 describes the equations of the classical E-PI model and modifications that are made to include the effect of gradient wind imbalance. Section 3 presents results from the slab boundary model across a wide parameter range and demonstrates the scale dependence of the solutions. Section 4 summarizes the outcome of this study and discusses some important implications of our findings.

## 2. Model conception

In this section, we construct the unbalanced (i.e., not in gradient wind balance) slab boundary layer

model by building upon the E-PI model for a steady state tropical cyclone (Emanuel 1986) and the more recently modified E-PI model by Emanuel and Rotunno (2011).

### a. Governing equations of the E-PI model

The E-PI theory is built upon the following foundational equations (see Emanuel 1986, 1995).

- *Definition of potential radius at the top of the boundary layer*<sup>1</sup>

$$\frac{f}{2}R^2 = M_b = v_b r_b + \frac{f}{2}r_b^2. \quad (1)$$

- *Budget equation for boundary layer entropy of the inner region ( $R \leq R_m$ )*

$$u_b \left( \frac{\partial r_b}{\partial R} \right)^{-1} \frac{\partial \chi_b}{\partial R} = \frac{C_H}{H_b} V_b (\chi_s - \chi_b). \quad (2)$$

- *Budget equation for boundary layer tangential wind*

$$u_b f \left( \frac{r_b}{R} \frac{\partial r_b}{\partial R} \right)^{-1} = -\frac{C_D}{H_b} V_b v_b. \quad (3)$$

- *Entropy at the sea surface*

$$\chi_s = \chi_a^* - A_s P_s. \quad (4)$$

- *Boundary layer entropy of the outer region ( $R > R_m$ )*

$$\chi_{bo} = -A_o P_s, \quad (5)$$

where

$$P_s = R_d T_s \ln(p_s/p_a),$$

$$A_s = \frac{T_s - T_t}{T_s} + \frac{\chi_a^*}{R_d T_s (1 - h_a)},$$

$$A_o = \frac{T_s - T_t}{T_s} + \frac{\chi_a^* h_a}{R_d T_s (1 - h_a)},$$

and

$$\chi = (T_s - T_t)s.$$

Subscript notation is as follows: *b* indicates evaluation at the top of the boundary layer, *s* indicates evaluation at the sea surface, *t* indicates evaluation at the ambient tropopause, *o* denotes evaluation in the outer region, and

<sup>1</sup>The boundary layer top is defined here by the height where the frictional stress vanishes for the first time.

TABLE 1. E-PI model notation.

Notation	Meaning
$u$	Radial wind
$v$	Tangential wind
$r$	Physical radius
$M$	Specific angular momentum
$V$	Horizontal wind speed
$p$	Pressure
$T$	Temperature
$s$	Specific entropy
$R_d$	Specific gas constant of dry air
$h$	Relative humidity
$C_D$	Surface drag coefficient
$C_H$	Surface transfer coefficient for enthalpy
$H_b$	Boundary layer depth
$f$	Coriolis parameter

$a$  indicates evaluation in the boundary layer of the far-field environment. The asterisk denotes that the thermodynamic variable is considered at water vapor saturation. The potential radius of maximum gradient wind,  $R_m$ , defines the boundary between the inner and outer regions. We note that the effect of dissipative heating is not included in the budget equation (2) for boundary layer entropy. Further notation is given in Table 1.

For comparison, Frisius and Schönemann (2012) outlined and solved similar equations to rederive E-PI to examine the influence of nonzero CAPE. In doing so, they set the Coriolis parameter to zero and assumed gradient wind balance. Since the aim of the present work is to include gradient wind imbalance in the boundary layer, neither of these assumptions is made herein. Furthermore, we assume neutrality to slantwise convection. Thus, we disregard the effects of slantwise convective available potential energy (SCAPE) as is done in the classical E-PI theory. The model is constructed as follows.

The budget equations for the boundary layer, Eqs. (2) and (3), do not require gradient wind balance. These are equivalent to the corresponding slab boundary layer equations introduced by Smith (2003) for the case of vanishing entrainment from the free atmosphere above. The process of entrainment will be considered separately in section 3g.

Inserting Eq. (3) into the entropy budget equation (2) gives an equation that relates the radial entropy gradient to the air-sea discontinuity:

$$-\frac{r_b}{fR} v_b \frac{\partial \chi_b}{\partial R} = \frac{C_H}{C_D} (\chi_s - \chi_b). \quad (6)$$

The approximation

$$v_b r_b = \frac{f}{2} (R^2 - r_b^2) \approx \frac{f}{2} R^2 \quad (7)$$

is valid in the inner region since the physical radius is much smaller than the potential radius (e.g., Emanuel 1997). Therefore, E86 simplified the entropy budget equation by substituting the approximation (7) to eliminate  $r_b$ . We obtain

$$-\frac{R}{2} \frac{\partial \chi_b}{\partial R} = \frac{C_H}{C_D} (\chi_s - \chi_b). \quad (8)$$

An important cornerstone of E-PI is the assumption that SCAPE vanishes in the steady state vortex. As a result, the boundary layer entropy and the saturation entropy of the free atmosphere become identical so that we can set  $\chi_b = \chi^* \equiv \chi$ . Neglecting the pressure dependence of surface entropy by setting  $A_s = 0$  leads to the differential equation

$$-\frac{R}{2} \frac{\partial \chi}{\partial R} = \frac{C_H}{C_D} (\chi_a^* - \chi). \quad (9)$$

Then, the solution for the inner region becomes

$$\chi = \chi_a^* - C_i \left( \frac{R}{R_m} \right)^{2C_H/C_D} \quad \text{for } R \leq R_m, \quad (10)$$

where  $C_i$  denotes an integration constant, which will be determined below. This solution is also valid in cases where gradient wind imbalance arises in the simplified slab boundary layer model.

To consider the pressure dependence (i.e.,  $A_s > 0$ ), the surface pressure must be determined. In E86 this has been done by solving the gradient wind balance equation. It is not valid to do this for the unbalanced case. However, if the balanced surface pressure field were to be inserted into Eq. (4), the resulting PI would be underestimated since the angular momentum surfaces are displaced toward the center by supergradient winds and the lower surface pressure there enhances the capacity to absorb moisture from the sea surface. As we are mainly interested in the qualitative description of superintensity by gradient wind imbalance, in the present study we will neglect the impact of the pressure dependence of surface entropy from the outset. We note that both the maximum unbalanced, and the gradient tangential, wind become stronger when taking into account  $A_s > 0$ . In turn, the pressure dependence of surface entropy is expected to have a rather small and, for the purpose of a qualitative study, negligible effect on the difference between  $v_{\max}$  and  $v_{g,\max}$  (i.e., maximum gradient wind). Therefore, we only describe the primary effect of gradient wind imbalance in this study.

Boundary conditions are needed to obtain the integration constant  $C_i$  in Eq. (10). In E86 the boundary

layer entropy of the outer region has been prescribed by assuming a constant relative humidity. The result of making such an assumption is that the radial decrease of  $\chi_b$  would only be due to the pressure dependence of surface entropy: however, we have already excluded this effect by our choice to neglect this pressure dependence. We prescribe the radial entropy profile in analogy to the wind profile derived in E86 [cf. his Eq. (48)] by

$$\chi = C_o \left( \frac{R}{R_m} \right)^{-\mu} \quad \text{for } R > R_m, \quad (11)$$

where  $\mu$  is the exponent describing the radial decay of entropy. In E-PI it is given by  $\mu = 4(1 - A_0)/A_0$  [cf. Eq. (17) in Frisius and Schönemann (2012)]. We do not fix the exact value here because the assumptions of constant relative humidity and constant temperature in the boundary layer of the outer region cannot be justified on physical grounds. Instead, we leave  $\mu$  as an unspecified parameter and note that it might be specified by numerical simulations or further new theoretical considerations. The continuity of entropy and the entropy gradient at  $R = R_m$  can be used to determine  $C_i$  and  $C_o$ . This leads us to the complete solution

$$\chi = \begin{cases} \chi_a^* - \frac{\mu \chi_a^*}{2C_H/C_D + \mu} \left( \frac{R}{R_m} \right)^{2C_H/C_D}, & R \leq R_m \\ \chi_a^* \frac{2C_H/C_D}{2C_H/C_D + \mu} \left( \frac{R}{R_m} \right)^{-\mu}, & R > R_m, \end{cases} \quad (12)$$

where  $\chi = \chi_b = \chi^*$ . It is possible to determine the central surface pressure from the hydrostatic equation since the physical and potential radii are identical at the vortex axis. Hence, the degree of gradient wind imbalance has no effect on central pressure when the pressure dependence of surface entropy is neglected. The model explicitly excludes eye dynamics (Emanuel 1995). If we were to consider eye dynamics, the entropy within the eye would become larger than that of the sea surface and gradient wind imbalance might contribute to an entropy increase due to additional subsidence.

*b. Inclusion of gradient wind imbalance*

To determine the unbalanced tangential boundary layer wind, further assumptions are made.

- (i) The gradient wind imbalance vanishes everywhere at a certain height  $z = z_g$  above the boundary layer.
- (ii) The integrated thermal wind balance equation is satisfied at this height. Hence, any possible gradient

wind imbalance that may occur above this level has no net effect on the thermal wind balance. Therefore, the impact of super- and subgradient winds above  $z = z_g$  must cancel each other. The gradient wind imbalance below this level does not violate the thermal wind balance equation in any case.

- (iii) Baroclinic effects are neglected below  $z = z_g$ . Therefore, the radial pressure gradient force is vertically constant for  $z < z_g$ .

The numerical experiment by BR09 demonstrates that assumption (i) is almost satisfied at a height of about 3 km in the eyewall and everywhere in the free troposphere above the boundary layer in the ambient region (see their Fig. 10). With assumption (ii), the possible effect of gradient wind imbalance above  $z = z_g$  is neglected throughout the entire domain. Although sub- and supergradient winds may occur owing to an oscillation along an angular momentum surface (see Fig. 10 in BR09), it is not clear if their effect is zero in the vertical average. However, this issue is beyond the scope of this study. With assumption (iii), the pressure gradient force at  $z = z_g$  becomes identical to that in the underlying boundary layer in physical space. This consequence does not apply in potential radius space however, so the solution must be transformed into physical space.

We now introduce the integrated thermal wind balance equation (for a derivation, see E86) that will be applied at the height of gradient wind balance ( $z = z_g$ ):

$$\frac{1}{r_g^2} = -\frac{2}{f^2 R^3} \frac{\partial \chi^*}{\partial R}, \quad (13)$$

where the index  $g$  refers to evaluation at  $z = z_g$  and  $\chi^* = (T_g - T_i)s^*$ . This equation relates the physical radius  $r_g$  to the radial entropy gradient. This is a good approximation when the outflow radius  $r_i$  is large compared to  $r_g$  (for more details, see E86). The tangential wind  $v_g$  at height  $z_g$  is provided by the definition of potential radius  $R^2 = r_g^2 + 2v_g r_g / f$ , which yields

$$\begin{aligned} v_g &= \left( -\frac{R}{2} \frac{\partial \chi^*}{\partial R} \right)^{1/2} - \frac{f^2 R^2}{4} \left( -\frac{R}{2} \frac{\partial \chi^*}{\partial R} \right)^{-1/2} \\ &= v_c - \frac{f^2 R^2}{4} \frac{1}{v_c}, \end{aligned} \quad (14)$$

where

$$v_c = \left( -\frac{R}{2} \frac{\partial \chi^*}{\partial R} \right)^{1/2} \quad (15)$$

would be identical to the cyclostrophic wind if the Coriolis force was absent. Note that the potential radius

already includes planetary rotation. Therefore,  $v_c$  is not exactly the cyclostrophic wind if  $f \neq 0$ . The approximation  $v_g \approx v_c$  is acceptable near the radius of maximum winds (RMW) for Rossby numbers typically found in the inner core of a tropical cyclone (Willoughby 2011):  $v_c$  can be obtained by inserting solution (12) into Eq. (15) as

$$v_c = \begin{cases} v_{g,\max} \left( \frac{R}{R_m} \right)^{C_H/C_D}, & R \leq R_m \\ v_{g,\max} \left( \frac{R}{R_m} \right)^{-\mu/2}, & R > R_m, \end{cases} \quad (16)$$

where

$$v_{g,\max} = \sqrt{\frac{(C_H/C_D)\mu}{2(C_H/C_D) + \mu} \frac{T_g - T_t}{T_s - T_t} \chi_a^*}. \quad (17)$$

For later application, it is necessary to transform the solution into physical space. The transformation can be accomplished using the thermal wind balance equation (13). The result is

$$\frac{R}{R_m} = \begin{cases} \left( \frac{r}{r_m} \right)^{1/(2-C_H/C_D)}, & R \leq R_m \\ \left( \frac{r}{r_m} \right)^{2/(4+\mu)}, & R > R_m, \end{cases} \quad (18)$$

where  $r_m = fR_m^2/(2v_{g,\max})$  is approximately equal to the radius of the gradient wind maximum and thus can be identified with the RMGW in the following. Therefore, with Eq. (18) we obtain the gradient wind profile in physical space at and below  $z = z_g$ ,

$$v_g = \begin{cases} v_{g,\max} \left( \frac{r}{r_m} \right)^{1/(2C_D/C_H-1)} - \frac{fr}{2}, & r \leq r_m \\ v_{g,\max} \left( \frac{r}{r_m} \right)^{-\beta} - \frac{fr}{2}, & r > r_m, \end{cases} \quad (19)$$

where  $\beta = \mu/(4 + \mu)$  is the so-called modified Rankine decay parameter (Mallen et al. 2005). For typical TCs, the potential intensity is approximately given by  $v_{g,\max}$  so long as  $fr_m \ll v_{g,\max}$ . Far away from the vortex center, however, the term  $fr$  becomes dominant. We can obtain the outer radius  $r_o$  by solving the above expression for  $v_g = 0$ :

$$r_o = (2Ro)^{1/(1+\beta)} r_m. \quad (20)$$

Here  $Ro = v_{g,\max}/(fr_m)$  denotes the local Rossby number here at the RMGW, that is, at  $r = r_m$ . For  $Ro \approx 1$  the vortex structure becomes very unrealistic since  $r_o$  and  $r_m$  are similar. Furthermore, approximation (7) becomes invalid in this case. We conclude that  $Ro \gg 1$  must be fulfilled so as to properly apply the model. Beyond  $r_o$  the tangential wind approaches the profile  $-fr/2$ . To maintain gradient wind balance, this anticyclonic solid body rotation would have to be balanced by an unrealistic surface pressure drop in the environment of the storm. Therefore, calculation of  $v_g$  is not reasonable beyond  $r = r_o$ .

Assumption (iii) allows us to set the gradient wind  $v_g$  identical to that inside the boundary layer, that is,  $v_{b,g} = v_g$ . The slab boundary layer model used here is based on that of Smith (2003) without entrainment of momentum by downwelling. The associated momentum equations [cf. Eqs. (13) and (14) of Smith (2003)] are given by

$$u_b \frac{\partial u_b}{\partial r} = -\frac{v_g^2 - v_b^2}{r} - f(v_g - v_b) - \frac{C_D}{H_b}(u_b^2 + v_b^2)^{1/2} u_b \quad (21)$$

and

$$u_b \frac{\partial v_b}{\partial r} = -\left( \frac{v_b}{r} + f \right) u_b - \frac{C_D}{H_b}(u_b^2 + v_b^2)^{1/2} v_b. \quad (22)$$

Note that the boundary layer equation for tangential momentum (22) is identical to Eq. (3) when potential radius instead of physical radius is used as radial coordinate.

The governing equations of this model show that the maximum supergradient wind depends upon seven parameters:  $v_{g,\max}$ ,  $r_m$ ,  $C_H$ ,  $C_D$ ,  $\beta$ ,  $H_b$ , and  $f$ . The number of parameters can be reduced by introducing nondimensional variables. With  $r = r_m \tilde{r}$  and  $(u, v) = v_{g,\max}(\tilde{u}, \tilde{v})$ , we get the following nondimensional boundary layer equations:

$$\tilde{u}_b \frac{\partial \tilde{u}_b}{\partial \tilde{r}} = -\frac{\tilde{v}_g^2 - \tilde{v}_b^2}{\tilde{r}} - \frac{\tilde{v}_g - \tilde{v}_b}{Ro} - \tilde{C}_D(\tilde{u}_b^2 + \tilde{v}_b^2)^{1/2} \tilde{u}_b \quad (23)$$

and

$$\tilde{u}_b \frac{\partial \tilde{v}_b}{\partial \tilde{r}} = -\left( \frac{\tilde{v}_b}{\tilde{r}} + \frac{1}{Ro} \right) \tilde{u}_b - \tilde{C}_D(\tilde{u}_b^2 + \tilde{v}_b^2)^{1/2} \tilde{v}_b, \quad (24)$$

where  $\tilde{C}_D = C_D r_m / H_b$ . The formula for the non-dimensional gradient wind becomes

$$\tilde{v}_g = \begin{cases} \tilde{r}^{1/(2C_D/C_H-1)} - \frac{1}{2\text{Ro}}\tilde{r}, & \tilde{r} < 1 \\ \tilde{r}^{-\beta} - \frac{1}{2\text{Ro}}\tilde{r}, & \tilde{r} \geq 1. \end{cases} \quad (25)$$

Now we have only four nondimensional parameters, namely  $\text{Ro}$ ,  $\tilde{C}_D$ ,  $\beta$ , and  $C_H/C_D$ . Since the RMGW influences both  $\text{Ro}$  and  $\tilde{C}_D$ , the boundary layer solutions may be very sensitive to the RMGW. From these parameters, it is possible to define two length scales, either of which may have importance to the solution: 1)  $H_b/C_D$  and 2)  $v_{g,\text{max}}/f$ . Therefore, the PI based on the unbalanced tangential wind depends upon the scale of the TC. On the other hand, the gradient wind resulting from E-PI theory is scale independent. This result arises from Eq. (17) and has also been shown from the more accurate analysis of E86.<sup>2</sup>

*c. Modified E-PI*

Emanuel and Rotunno (2011) improved the E-PI model by including a variable outflow temperature  $T_o$ . The original E-PI assumption of a constant  $T_o \equiv T_i$  is at odds with the fact that isentropes of the outflow do not approach the same absolute temperature. This would only be a reasonable assumption in the lower stratosphere. Instead of a constant  $T_o$ , they assumed a critical outflow Richardson number to derive the outflow temperature. Besides being more realistic, this modification has the advantage of making obsolete the ad hoc assumption that relative humidity is constant in the boundary layer of the outer region.

Apart from a nonconstant outflow temperature, the modified E-PI model is based on the same relations used in the classical E-PI theory. Furthermore, Emanuel and Rotunno also neglected the pressure dependence of surface entropy. In this context, solution (10) is valid in the complete vortex that extends out to the outer radius  $r_o$  where the tangential wind vanishes. In a similar way, we can incorporate the solution into the slab boundary layer model. The profile of the angular momentum at  $z = z_g$  of the modified E-PI solution is given by [cf. Eq. (36) of Emanuel and Rotunno (2011)]:

$$\left(\frac{M_g}{M_m}\right)^{2-C_H/C_D} = \frac{2(r/r_m)^2}{2 - C_H/C_D[1 - (r/r_m)^2]}, \quad (26)$$

where  $M_m$  is the angular momentum at the RMGW. A derivation of this solution is given in the appendix. With the modified solution the gradient wind at  $z = z_g$  is given as

$$v_g = v_{g,\text{max}} \frac{r_m}{r} \left\{ \frac{2(r/r_m)^2}{2 - (C_H/C_D)[1 - (r/r_m)^2]} \right\}^{1/(2-C_H/C_D)} - \frac{1}{2} fr, \quad (27)$$

where we made the approximation  $M_g \approx v_{g,\text{max}}r_m$ . The distinction between inner and outer region is not necessary since the solution holds throughout the entire vortex. The maximum gradient wind  $v_{g,\text{max}}$  depends on environmental parameters in a different way than the classical E-PI. It is given by [cf. Eqs. (40) and (41) of Emanuel and Rotunno (2011)]; for a derivation see the appendix]:

$$v_{g,\text{max}} = \left[ \frac{C_H}{C_D} \left( \frac{1}{2} \frac{C_H}{C_D} \right)^{1/(2C_D/C_H-1)} \frac{T_g - T_i}{T_s - T_i} \chi_a^* \right]^{1/2}. \quad (28)$$

In nondimensional terms the gradient wind for modified E-PI can be written as

$$\tilde{v}_g = \frac{1}{\tilde{r}} \left[ \frac{2\tilde{r}^2}{2 - C_H/C_D(1 - \tilde{r}^2)} \right]^{1/(2-C_H/C_D)} - \frac{1}{2\text{Ro}}\tilde{r}. \quad (29)$$

At some radius  $\tilde{r} = \tilde{r}_o$  the tangential wind becomes zero. With  $\tilde{r}_o^2 C_H/C_D \gg 2 - C_H/C_D$ , the radius of vanishing tangential wind is approximately given by

$$\tilde{r}_o \approx \left[ 2\text{Ro} \left( 2 \frac{C_D}{C_H} \right)^{1/(2-C_H/C_D)} \right]^{1/2}. \quad (30)$$

Note that the nondimensional gradient wind of the modified E-PI solution only depends upon  $C_H/C_D$  and  $\text{Ro}$ . Therefore, when the slab boundary layer model is coupled to the modified E-PI solution, there are only three nondimensional parameters: the Rossby number  $\text{Ro}$ , the drag coefficient  $\tilde{C}_D$ , and the ratio of the transfer coefficients  $C_H/C_D$ . Also, note that modified E-PI still does not depend on the RMGW value [cf. Eq. (28)].

*d. Inclusion of horizontal diffusion*

Horizontal momentum exchange by small-scale eddies plays an important role in the inner core of a tropical cyclone. Emanuel (1997) pointed out that this process prevents the formation of a discontinuity in the eyewall region. Rotunno and Bryan (2012) found that the intensity declines and that the RMW increases with

<sup>2</sup>The scale independence becomes evident by combination of Eqs. (43) and (46) of E86.

increasing horizontal diffusion. It is beyond the scope of this study to directly account for the horizontal turbulent mixing throughout the troposphere in the calculation of the flow in the model. Possibly, horizontal mixing has an effect on the unknown modified Rankine decay parameter  $\beta$ , but the numerical calculations by Rotunno and Bryan indicate that the tangential wind profile is rather insensitive to horizontal mixing outside the RMW.

In the boundary layer model we can incorporate horizontal turbulent exchange of momentum by adding the terms

$$D_u = \frac{2}{\tilde{r}} \frac{\partial}{\partial \tilde{r}} \left( \nu_h \tilde{r} \frac{\partial \tilde{u}_b}{\partial \tilde{r}} \right) - 2\nu_h \frac{\tilde{u}_b}{\tilde{r}^2} \quad (31)$$

and

$$D_v = \frac{1}{\tilde{r}^2} \frac{\partial}{\partial \tilde{r}} \left[ \nu_h \tilde{r}^2 \left( \frac{\partial \tilde{v}_b}{\partial \tilde{r}} - \frac{\tilde{v}_b}{\tilde{r}} \right) \right] \quad (32)$$

to Eqs. (23) and (24), respectively. The nondimensional turbulent exchange coefficient  $\nu_h$  is parameterized by

$$\nu_h = \frac{l^2}{r_m^2} \left[ \left( \frac{\partial \tilde{v}_b}{\partial \tilde{r}} - \frac{\tilde{v}_b}{\tilde{r}} \right)^2 + 2 \left( \frac{\partial \tilde{u}_b}{\partial \tilde{r}} \right)^2 + 2 \frac{\tilde{u}_b^2}{\tilde{r}^2} \right]^{1/2}, \quad (33)$$

where  $l$  denotes the horizontal mixing length. This parameterization is in agreement with the approach by Rotunno and Bryan (2012) and it introduces a new nondimensional parameter, namely, the nondimensional horizontal mixing length  $\tilde{l} = l/r_m$ .

### e. Solution method

We solve the system equations (that exclude horizontal diffusion) by integrating inward from  $\tilde{r} = \tilde{r}_o$  toward the center until the radial wind becomes zero. At this radius, the inflow breaks down and the air moves upward into the eyewall. Since the vertical velocity is typically upward in this region, it is acceptable to neglect the entrainment term of the original model. In the outer region the vertical motion is characterized by areas of both upward and downward motion, so entrainment could have an appreciable effect. Since the wind in the free troposphere of the outer region is balanced, vertical momentum fluxes in this region act to push the tangential boundary layer wind toward gradient wind balance. We keep this in mind and compare the results with solutions where such an effect is included in section 3g. We set  $\tilde{v}_b = \tilde{v}_g = 0$  and  $\tilde{u}_b = -0.02$  at  $\tilde{r} = \tilde{r}_o$ . The weak radial inward flow is necessary to push the air toward the center. Without this inflow, the low pressure gradient force would not be strong enough to overcome the restoring inertial force. When horizontal small-scale

mixing is incorporated (see next paragraph), a boundary condition at  $\tilde{r} = \tilde{r}_o$  is not required since the boundary layer solution evolves in a time-dependent model even beyond  $\tilde{r} = \tilde{r}_o$ . Note that at  $\tilde{r} = 1$  the vorticity of gradient wind drops to a lower value. This vorticity drop is the main reason for the occurrence of supergradient winds because the radial wind cannot adjust immediately to the lower value. In turn, gradient wind balance cannot be maintained here.

A more elaborate solution technique becomes necessary when horizontal diffusion is included. In this case, we cannot solve the time-independent equations by an inward radial integration since the boundary conditions for the Reynolds stresses at  $\tilde{r} = \tilde{r}_o$  are unknown. Therefore, we solve the full time-dependent equations until a steady-state solution emerges. For this purpose, we choose a model domain extending from  $\tilde{r} = 0$  to  $\tilde{r} = 200$  and divide it into 8000 grid points. Radial and tangential wind grid points are staggered and the leapfrog scheme is applied for time integration. The gradient wind is set to zero beyond the radius  $\tilde{r}_o$  so as to obtain realistic solutions.

## 3. Results

In this section, we present calculations made with the slab boundary layer model. First, the model is forced by the original E-PI solution. The forcing by the modified E-PI solution will be discussed later on in section 3h. The standard parameters are  $\beta = 0.8$ ,  $\text{Ro} = 120$ ,  $C_H/C_D = 1$ , and  $\tilde{C}_D = 0.02$ . Reasonable dimensional values leading to this parameter set are given by  $r_m = 10$  km,  $f = 0.5 \times 10^{-4} \text{ s}^{-1}$ ,  $v_{g,\text{max}} = 60 \text{ m s}^{-1}$ ,  $H_b = 1500$  m, and  $C_D = 0.003$ . Figure 1 displays the radial and tangential boundary layer winds and the gradient wind as a function of physical radius for the standard configuration. As can be seen, the tangential wind is subgradient outside the eyewall and becomes supergradient in the inner region. At the boundary between the inner and outer regions, gradient wind balance is almost exactly satisfied. Inside this boundary, superintensity reaches values of about 18%. The results are qualitatively similar to those obtained from numerical simulations with axisymmetric cloud models by BR09 (see their Fig. 3) and Frisius and Schönemann (2012). The radial inflow velocity attains a nondimensional value of about 0.35 at the radius of maximum gradient wind. This gives a reasonable inflow angle of about  $19^\circ$  [cf. Fig. 17 in Frank (1977)] using the formula  $\alpha = \arctan(-\tilde{u}_b/\tilde{v}_b)$ . At the radius of maximum tangential wind the radial velocity vanishes and air rises vertically into the eyewall.

For comparison, Fig. 2 displays radial profiles of the tropical cyclone simulation reference experiment

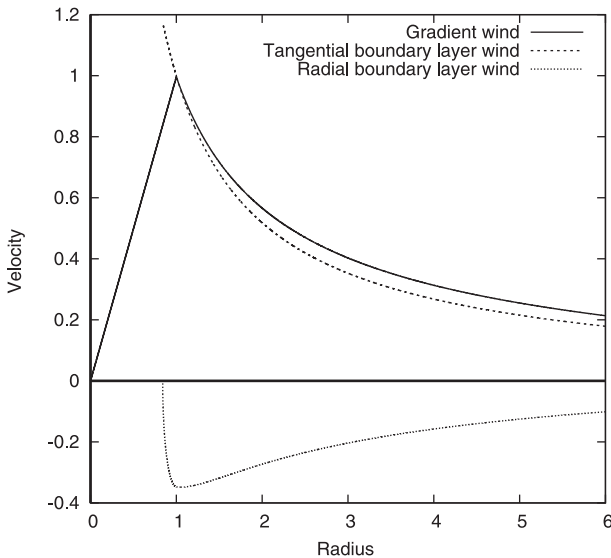


FIG. 1. Radial profiles of gradient wind (solid line), tangential boundary layer wind (dashed line), and radial boundary layer wind (dotted line) of the reference solution for the slab boundary layer model: all values are nondimensional.

(REF) with the axisymmetric cloud hurricane model (HURMOD). The numerical experiment is comprehensively described in Frisius and Schönemann (2012). The figure shows the vertically averaged radial and tangential winds in the boundary layer at  $t = 140$  h of the simulation. The figure also shows the gradient wind at the height where the gradient wind imbalance approximately vanishes ( $z = 2.5$  km); here the gradient wind is nearly maximized. For sake of comparison, a profile ( $v \sim r^{-0.875}$ ) has been fitted to the gradient wind near the outer edge of the eyewall. The relative difference between the RMGW and the RMW is larger in HURMOD than in the slab boundary layer model. The boundary layer tangential wind is slightly subgradient outside the eyewall but becomes supergradient inside the RMGW; in contrast to the slab boundary model it is slightly subgradient at the RMGW. In HURMOD the breakdown of the radial inflow is smooth and the radius of vanishing radial wind appears inward of the RMW. This is in contrast to the slab boundary model in which the breakdown is rather abrupt and takes place exactly at the RMW. While the slab boundary layer model makes no prediction of the flow inside the eye, HURMOD reveals radial winds that nearly vanish. This may possibly be due to the strongly sheared balanced tangential wind profile. Strong wind shear results in an enhanced vorticity and presumably also a higher inertial stability, which may act like a wall to inhibit the inflow. The gradient wind outside the eyewall is roughly proportional to  $r^{-0.875}$ . Therefore, with respect to the axisymmetric HURMOD

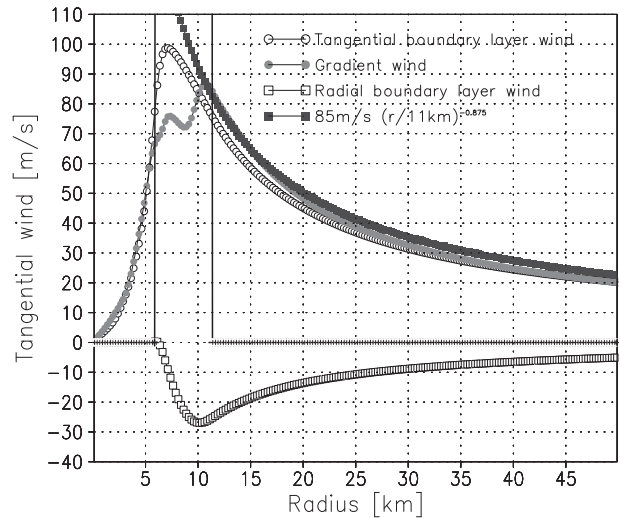


FIG. 2. Radial profiles taken from the HURMOD simulation of a superintense tropical cyclone. Displayed are vertically averaged tangential boundary layer wind (open circles), radial boundary layer wind (open squares), gradient wind at  $z = 2.5$  km (gray filled circles), and the analytical profile  $v(r) = 85 \text{ m s}^{-1} \times (r/11 \text{ km})^{-0.875}$  (dark gray filled squares). The vertical average is taken from the bottom to a height of 1125 m. The vertical lines enclose the eyewall region where vertical velocity at  $z = 1062.5$  m is larger than  $0.5 \text{ ms}^{-1}$ .

simulation,  $\beta = 0.8$  is more suitable than the value found by E86 ( $\beta = 0.542$ ). We note, however, that the decay parameter found in HURMOD is higher than that found in observational studies, which typically ranges between 0.5 and 0.7 for strong storms Mullen et al. (2005). At this point, we can only hypothesize that the deviation from observed  $\beta$  values may possibly be due to the absence of any nonaxisymmetric flow features and the simplified cloud microphysics in HURMOD.

In the following subsections we investigate the sensitivity of the boundary layer model to 1) the RMGW, 2) the Rossby number  $Ro$ , and 3) the modified Rankine decay exponent  $\beta$ . While we also examined the sensitivity of the model to  $C_H/C_D$ , the influence of  $C_H/C_D$  on supergradient winds was found to be small. At first glance this may appear contradictory to the results from more complex models. Bryan (2012) found a decrease of superintensity with increasing  $C_H/C_D$  (see his Fig. 11). There are two possible reasons for this discrepancy. First, we used a fixed decay exponent  $\beta$ , which possibly depends sensitively on  $C_H/C_D$ . Second, Bryan varied  $C_D$  and kept  $C_H$  constant and, therefore,  $C_D$  decreases with  $C_H/C_D$ . This is different from our procedure since we leave  $C_D$  constant when we vary  $C_H/C_D$ . Indeed, we will see that the results of Bryan (2012) are consistent with ours since an increase of  $C_D$  leads to larger supergradient winds in our model (see below).

### a. Sensitivity to RMGW

By varying  $Ro$  and  $\tilde{C}_D$  together, the dependence of the boundary layer flow to RMGW can be examined. We investigate the sensitivity to this dimensional parameter in addition to the nondimensional ones, since the RMGW is a measure for the tropical cyclone's size—a property of considerable interest in ongoing research. Figure 3 displays the results obtained from Eqs. (23) and (24) for unbalanced radial and tangential wind velocity with  $r_m = 5$  km,  $r_m = 10$  km,  $r_m = 50$  km, and  $r_m = 200$  km normalized to maximum gradient wind in the reference setup. For a vortex with  $r_m = 5$  km the radial inflow is very weak with only small wind imbalance. For a storm with a RMW this small, gradient wind balance is nearly satisfied in the outer region ( $\tilde{r}_m > 1$ ) because momentum advection and drag only attain small magnitudes. As a further consequence of the weak inflow and the small inertia, no notable supergradient winds arise and the inflow even breaks down outside the RMGW. Hence, we do not obtain a realistic solution when  $r_m \leq 5$  km. Furthermore, in a 3D tropical cyclone model, Xu and Wang (2010) found that a storm with a radius of maximum near-surface winds of only 7.5 km is considerably weaker than storms with near-surface RMWs between 12.5 and 22.5 km. They reasoned that too-small storms grown from a small initial vortex do probably never form a strong TC. We observe an increased radial inflow strength in the outer region with increasing RMGW radius values. This leads to significant subgradient boundary layer winds in the outer region. Superintensity due to the supergradient wind is strongest for  $r_m = 50$  km. Two competing effects determine the degree of superintensity: 1) superintensity is supported by the inertia of the radial inflow and 2) it is weakened by the degree of subgradient wind imbalance outside the RMGW. The latter effect dominates for large RMGW values. For  $r_m = 50$  km and  $r_m = 200$  km, the inflow angle attains unrealistically high values at the RMGW ( $\sim 45^\circ$ ) while for  $r_m = 5$  km the inflow breaks down outside of the RMGW. For large RMGW values the radial extent of the outer region is unnaturally small compared to that of the inner core. This is a consequence of the small Rossby number; cf. Eq. (20). These results reveal a very large sensitivity with respect to the scale of the tropical cyclone. This leads to the following question: can a steady-state tropical cyclone only survive in a parameter range where the boundary layer flow characteristics correspond to typically observed conditions (inflow angle, degree of gradient wind imbalance)? From the aforementioned results we can deduce the following: a tropical cyclone cannot be as small as a waterspout because the boundary layer inflow is much too weak. On the other hand, unless there is considerable external

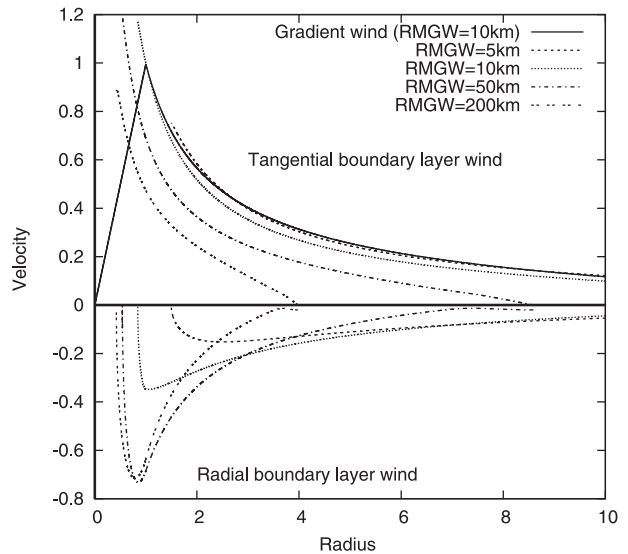


FIG. 3. Radial profiles of tangential boundary layer wind (above the zero axis) and radial boundary layer wind (below the zero axis) for different RMGW values:  $r_m = 5$  km (dashed lines),  $r_m = 10$  km (dotted lines),  $r_m = 50$  km (dash-dotted lines), and  $r_m = 200$  km (double-dashed lines). The solid line displays the gradient wind for  $r_m = 10$  km and all values are nondimensional, normalized to maximum gradient wind in the reference setup.

baroclinic forcing, such as occurs during extratropical transition events [e.g., Hurricane Sandy (2012)], a tropical cyclone cannot be as large as a synoptic-scale cyclone because the near-surface air suffers substantial frictional losses along the extended inflow trajectory and, thus, cannot spin up enough angular momentum. Therefore, the range of observed TC scales seems to be related to boundary layer dynamics. The relevant horizontal length scales for the slab boundary layer are  $v_g/f = 1200$  km and  $H_b/C_D = 500$  km. The latter length scale gives a consistent explanation of why tropical cyclones arise and are maintained on the meso- $\alpha$  scale (200–2000 km; e.g., Cotton and Anthes 1989). The length scale  $v_g/f$  does, on the other hand, also play an important role for tropical cyclone size. It prescribes its upper bound since for a larger size the frictional dissipation, which is necessary to move the air out of the outflow anticyclone, is larger than the energy that can be supplied by a Carnot cycle (Emanuel 1989). This argument cannot be comprehended in the present model, but we also have the limitation  $r_o < 2v_g/f$  to obtain a realistic vortex [cf. Eq. (20)]. Which one of these two length scales is more dominant for the size control will be investigated with HURMOD in a future study.

### b. Sensitivity to drag coefficient

Variations in the nondimensional drag coefficient  $\tilde{C}_D$  may lead to a similar response as variations in the

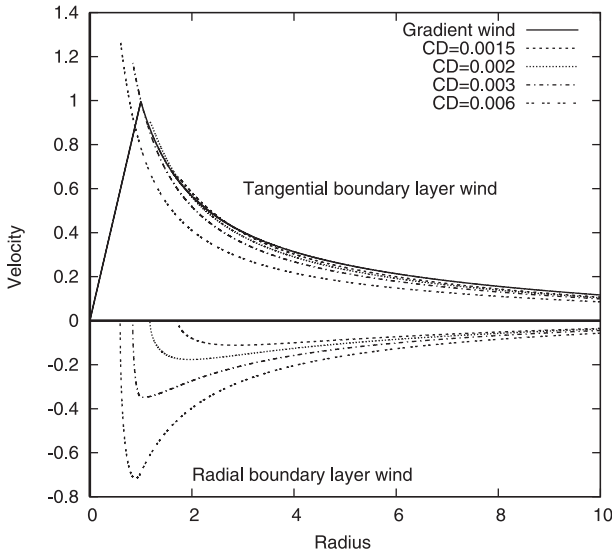


FIG. 4. Radial profiles of tangential boundary layer wind (above the zero axis) and radial boundary layer wind (below the zero axis) for different drag coefficients values:  $C_D = 0.0015$  (dashed lines),  $C_D = 0.002$  (dotted lines),  $C_D = 0.003$  (dash-dotted lines), and  $C_D = 0.006$  (double-dashed lines). The entropy transfer coefficient has been varied accordingly and the solid line displays the gradient wind. All values are nondimensional as in Fig. 3.

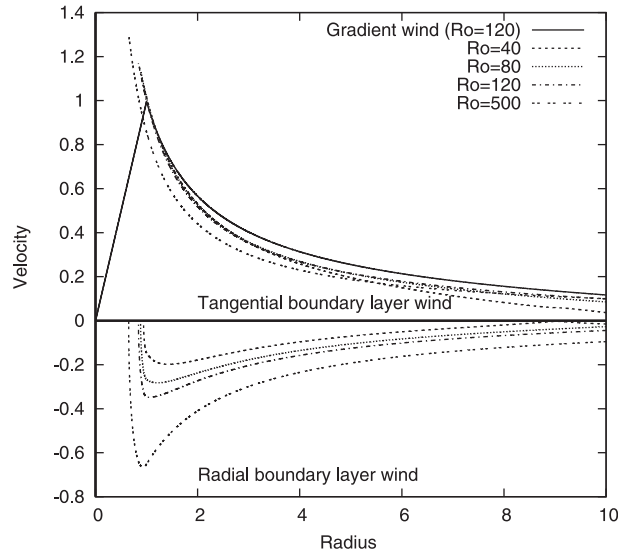


FIG. 5. Radial profiles of tangential boundary layer wind (above the zero axis) and radial boundary layer wind (below the zero axis) for different local Rossby numbers near the azimuthal wind maximum:  $Ro = 40$  (dashed lines),  $Ro = 80$  (dotted lines),  $Ro = 120$  (dash-dotted lines), and  $Ro = 500$  (double-dashed lines). The solid line displays the gradient wind for  $Ro = 120$  and all values are nondimensional as in Fig. 3.

RMGW because  $\tilde{C}_D \propto r_m$ . In the previous subsection, RMGW variations also lead to variations in  $Ro$ . In this subsection, we keep  $Ro$  fixed. Figure 4 shows radial profiles for the boundary layer flow for  $C_D = C_H = 0.0015$ ,  $C_D = C_H = 0.002$ ,  $C_D = C_H = 0.003$ , and  $C_D = C_H = 0.006$ . This corresponds to a variation of the nondimensional factor  $\tilde{C}_D$  since we are not varying  $C_D/C_H$  here. The results show that larger values of  $C_D$  lead to larger inflow velocities and supergradient winds. This is in accordance with the results shown in Fig. 3, in which the RMGW variation has a similar effect. The Rossby number also affects the outer radius  $r_o$ , as shown in the previous subsection and Eq. (20). In contrast, variations in  $\tilde{C}_D$  do not lead to changes in  $r_o$ . Therefore, the inflow region does not shrink relative to the RMGW as  $\tilde{C}_D$  is increased.

c. Sensitivity to Rossby number

Figure 5 shows profiles of boundary layer flow for local Rossby number values of  $Ro = 40$ ,  $Ro = 80$ ,  $Ro = 120$ , and  $Ro = 500$ . Assuming  $r_m = 10$  km and  $v_{g,max} = 60$   $\text{ms}^{-1}$  these values correspond roughly to the geographical latitudes  $90^\circ$ ,  $30^\circ$ ,  $20^\circ$ , and  $5^\circ\text{N}$ , respectively. As  $Ro$  increases, the winds become more strongly supergradient inside the RMGW, while they become more subgradient outside. This occurs because the inflow strength increases as  $Ro$  increases (Fig. 5). As a consequence, the largest superintensity arises for the

highest Rossby number ( $Ro = 500$ ). In this case, the inflow velocity becomes unrealistically large. To produce such a high Rossby number in the vicinity of the RMGW for these parameters requires  $f$  to be quite small. The corresponding latitude is about  $5^\circ\text{N}$ ; TCs are rarely observed at such low latitudes (e.g., Emanuel 2003).

d. Sensitivity to modified Rankine decay exponent  $\beta$

Figure 6 shows the sensitivity of the radial wind profiles to the modified Rankine decay exponent  $\beta$  for  $\beta = 0.65$ ,  $\beta = 0.7$ ,  $\beta = 0.8$ , and  $\beta = 0.9$ . The inflow is stronger and the maximum intensity is higher for larger values of  $\beta$ . This can be easily understood on the basis of Eq. (24), which can be written as

$$\tilde{u}_b = -\frac{\tilde{C}_D \tilde{v}_b^2}{\sqrt{\tilde{\zeta}_b^2 - \tilde{C}_D^2 \tilde{v}_b^2}}, \tag{34}$$

where  $\tilde{\zeta}_b$  is the nondimensional absolute boundary layer vorticity. Since vorticity decreases with increasing  $\beta$ , this equation shows that the radial velocity increases with  $\beta$ . For small  $\beta$  values  $< 0.8$  (as predicted by E-PI theory) superintensity vanishes. For such low  $\beta$  values, the inflow terminates outside the RMGW. For  $\beta = 0.542$ , the inflow cannot evolve in the present boundary layer model. This is the value predicted by the E-PI model

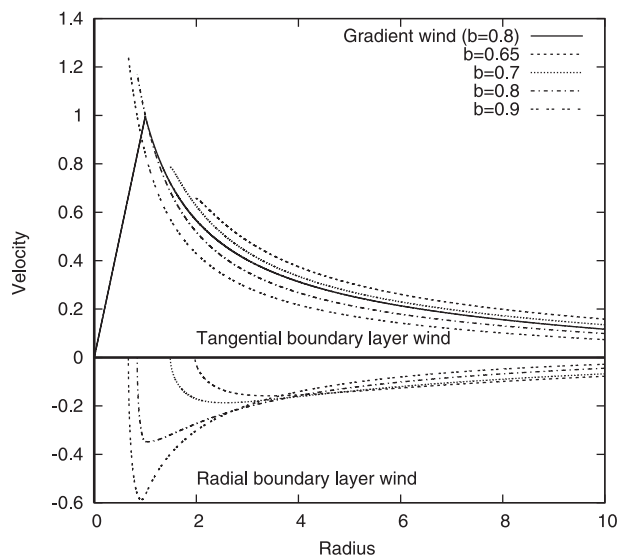


FIG. 6. Radial profiles of tangential boundary layer wind (above the zero axis) and radial boundary layer wind (below the zero axis) for different values of the profile parameter:  $\beta = 0.65$  (dashed lines),  $\beta = 0.7$  (dotted lines),  $\beta = 0.8$  (dash-dotted lines), and  $\beta = 0.9$  (double-dashed lines). The solid line displays the gradient wind for  $\beta = 0.8$  and all values are nondimensional as in Fig. 3.

(see E86) owing to the assumption of constant relative humidity in the outer region's boundary layer.

*e. Combined view*

In the previous subsection we only examined the sensitivity with respect to one parameter at a time; the others remain fixed. More information can be deduced by varying two parameters together; the results are shown in Fig. 7. The top panel of Fig. 7 shows the nondimensional superintensity as a function of  $\beta$  and RMGW. Nondimensional superintensity is defined as the maximum of tangential boundary layer wind minus the maximum gradient wind in nondimensional terms. The maximum superintensity occurs for  $\beta = 0.9$  at an RMGW of about 15 km. The RMGW at which superintensity maximizes is larger when the  $\beta$  value is small. No superintensity occurs for low  $\beta$  values and at smaller RMGW values. This result indicates the existence of an optimal RMGW for each value of  $\beta$ . The range of RMGW values for which superintensities exceed 20% corresponds to the typical range in observed tropical cyclones. The bottom panel of Fig. 7 shows nondimensional superintensity as a function of Rossby number and RMGW. Superintensity increases with increasing Rossby number, and the RMGW at maximum superintensity becomes larger with decreasing Rossby number. If it is true that the optimal RMGW is related to the RMGW value that reveals the largest supergradient winds, this result

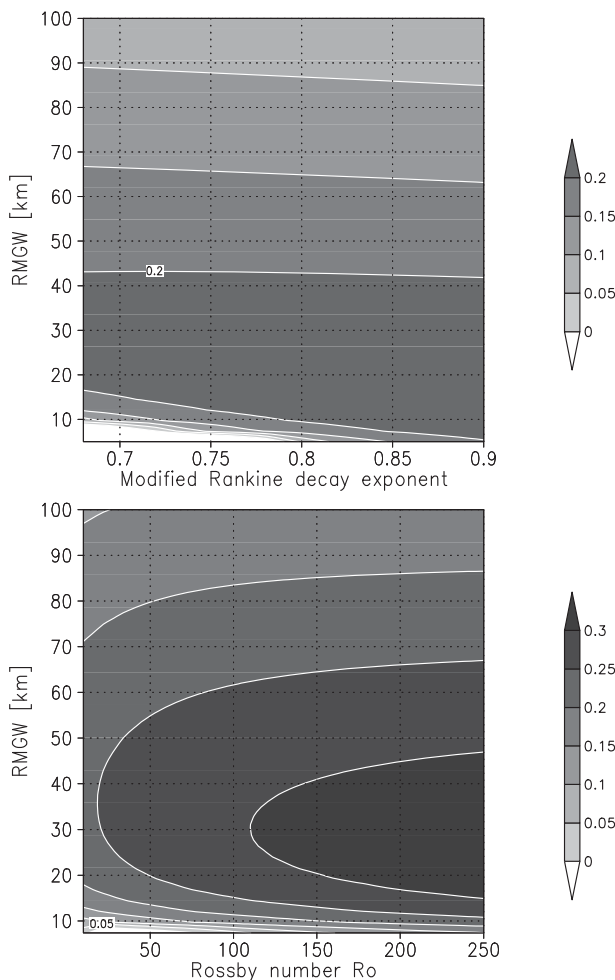


FIG. 7. Nondimensional superintensity as a function of (top) modified Rankine decay exponent  $\beta$  and RMGW and (bottom) local Rossby number  $Ro$  and RMGW.

suggests that storms should be smaller near the equator and larger at high latitudes. Furthermore, the degree of superintensity by gradient wind imbalance should decrease with latitude.

*f. Sensitivity to horizontal diffusion of momentum*

In this subsection, we present results from the slab boundary model that includes the effects of turbulent horizontal momentum diffusion. Figure 8 displays the boundary layer wind components as a function of radius for three different horizontal mixing lengths:  $l = 200$  m,  $l = 500$  m,  $l = 1000$  m, and  $l = 3000$  m. These mixing lengths correspond to the nondimensional values  $\tilde{l} = 0.02$ ,  $\tilde{l} = 0.05$ ,  $\tilde{l} = 0.1$ , and  $\tilde{l} = 0.3$ , respectively. The profiles outside the RMW are, except for the case  $l = 3000$  m, quite similar to the nondiffusive reference solution (cf. Fig. 1) albeit, with a slightly lower intensity. The

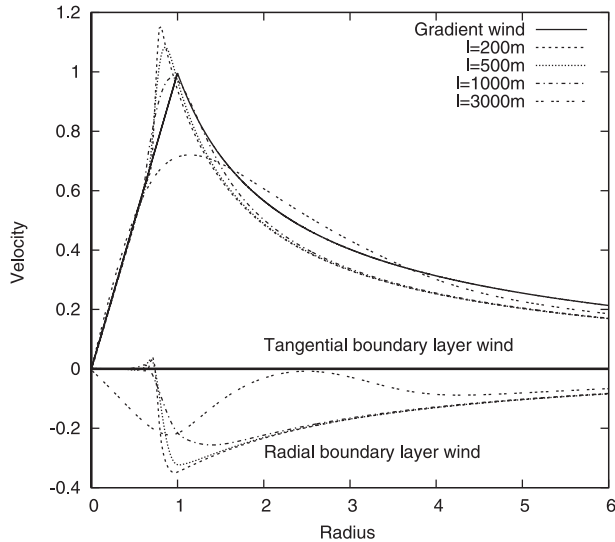


FIG. 8. Radial profiles of tangential boundary layer wind (above the zero axis) and radial boundary layer wind (below the zero axis) of the slab boundary model including horizontal diffusion. Shown are results for different values of horizontal mixing length:  $l = 200\text{ m}$  (dashed lines),  $l = 500\text{ m}$  (dotted lines),  $l = 1000\text{ m}$  (dash-dotted lines), and  $l = 3000\text{ m}$  (double-dashed lines). The solid line displays the gradient wind.

similarity of the two solutions suggests that the choice of the boundary condition at  $\tilde{r} = \tilde{r}_0$  in the nondiffusive model is reasonable. Now that turbulent horizontal diffusion is included in the boundary layer equations of motion, the tangential wind profile can be calculated inside the RMW. In the core, a small region with outward flow appears, but farther inward the radial flow nearly vanishes and the tangential wind is almost in gradient wind balance. Superintensity increases as the mixing length decreases and as the RMW shifts away from the RMGW. The inflow strength also weakens as the mixing length becomes larger. These results are in qualitative agreement with those of Rotunno and Bryan (2012), who found a similar response to horizontal diffusion in an axisymmetric cloud resolving model (see their Figs. 1 and 7). For  $l = 3000\text{ m}$  the solution considerably differs from the others. The maximum tangential wind attains a very low value of about 0.7 but outside the RMGW supergradient winds arise. The inflow strength exhibits two maxima and extends to the vortex axis. Such results were not obtained by Rotunno and Bryan. However, they used a full model in which horizontal diffusion also affects the thermodynamic fields and, hence, the gradient wind. Here, we kept the gradient wind as in the zero diffusion case and, therefore, we cannot expect a realistic result for large  $l$  values. Figures 9a and 9b show the sensitivity to the RMGW and  $\beta$ , respectively, for solutions with a mixing length of  $l = 500\text{ m}$ . The figures should be

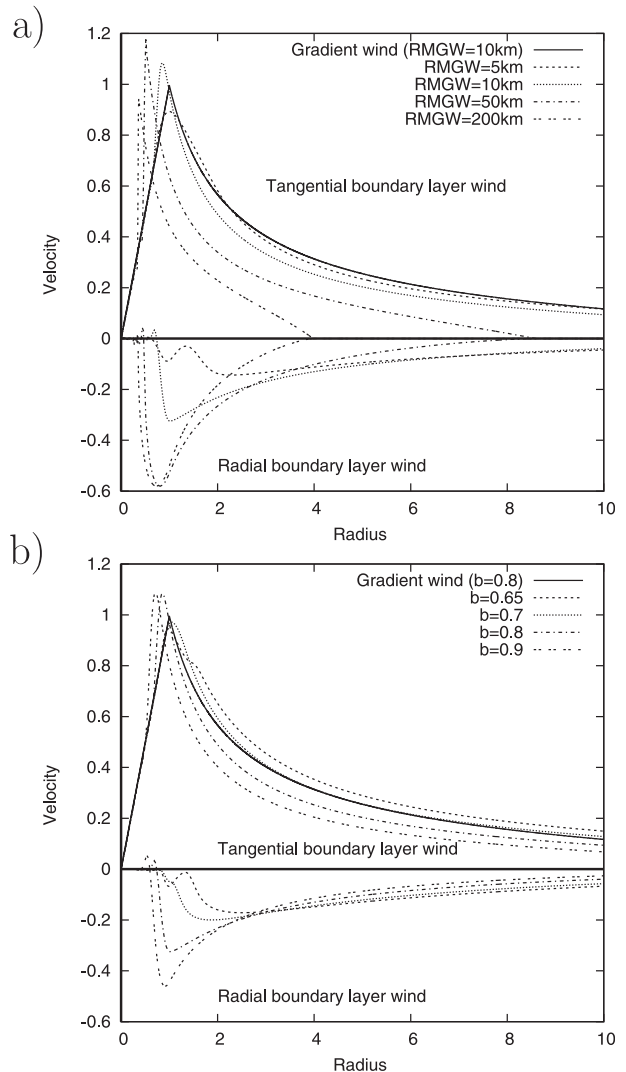


FIG. 9. (a) As in Fig. 3, but the solution includes horizontal diffusion with  $l = 500\text{ m}$ , and (b) as in Fig. 6, but the solution includes horizontal diffusion with  $l = 500\text{ m}$ .

compared to Figs. 3 and 6. The results with and without diffusion are qualitatively similar, but we note that the inflow outside the RMGW does not breakdown when horizontal diffusion is present. Instead, the radial wind profiles for these cases exhibit several inflection points. Furthermore, when the RMGW and  $\beta$  values are both large in the presence of horizontal diffusion, the inflow strength and superintensity are weaker than in the nondiffusive cases. As expected, we can conclude that horizontal diffusion has a weakening effect on the boundary layer wind intensity. Notwithstanding, the conclusions from the nondiffusive model appear to remain valid except inflow breakdown outside the RMGW becomes unlikely in the presence of significant radial turbulent diffusion.

### g. Sensitivity to entrainment of momentum in the outer region

So far, we have neither included vertical momentum advection by the cyclone-scale flow nor vertical mixing of momentum by shallow convection. However, these processes may be important in the outer region. Furthermore, downdrafts in spiral bands may affect the boundary layer and, therefore, the intensity, as found by Wang (2009). To simulate this vertical momentum transfer, we include the parameterization by Smith (2003). He calculates the vertical velocity  $w_b$  at the top of the boundary layer by solving the continuity equation. This gives

$$w_b = -H_b \frac{1}{r} \frac{\partial}{\partial r} (ru_b). \quad (35)$$

This vertical velocity contributes to the vertical entrainment by the large-scale flow. Moreover, shallow cumulus convection can also contribute to a vertical exchange of momentum. To consider this, Smith added a constant downward velocity  $w_{sc}$  from the shallow convection to  $w_b$ . Thus, the net downward vertical velocity at the top of the boundary layer becomes

$$w_- = \frac{1}{2} (w_b - |w_b|) - w_{sc}. \quad (36)$$

Of course the downward mass flux due to nonzero  $w_{sc}$  will be compensated by an upward mass flux of equal strength that, however, does not contribute to the momentum budget. The terms

$$\frac{w_-}{H_b} u_b \quad \text{and} \quad \frac{w_-}{H_b} (v_b - v_g) \quad (37)$$

are added to the rhs of Eqs. (21) and (22) for  $r > r_m$ , respectively. Inside the RMGW, this parameterization is not applied since the vertical flux into the eyewall dominates here. Effectively, these terms act as a relaxation to the balanced state  $v_b = v_g$  and  $u_b = 0$  with the time scale  $-H_b/w_-$ . Figure 10 displays the maximum tangential wind and radial wind profiles for several  $w_{sc}$  values. We see that both the inflow velocity and the maximum tangential wind decrease with increasing cumulus vertical velocity  $w_{sc}$ . This implies that vertical momentum exchange inhibits superintensity. For  $w_{sc} = 0$  the result is very similar to the solution without vertical momentum exchange. This shows, in agreement with Smith (2003), that entrainment by large-scale subsidence is negligible: Smith recommends a value near to  $w_{sc} = 0.02 \text{ m s}^{-1}$ . In this case superintensity is still significant and similar to the case without entrainment. Figure 10 also shows the

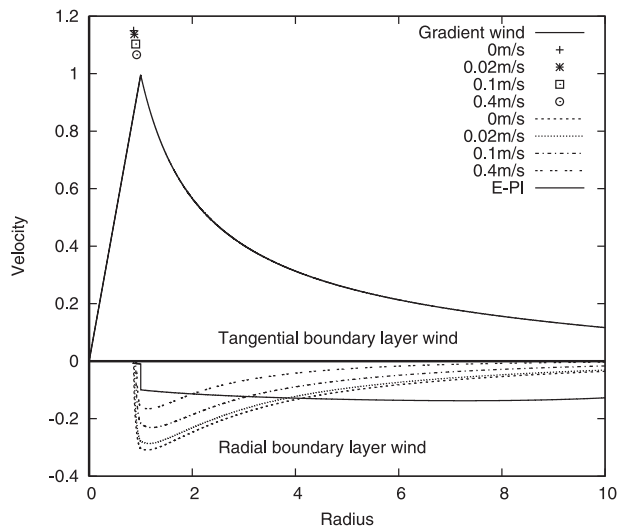


FIG. 10. Maximum of tangential boundary layer wind (above the zero axis), and profiles of radial boundary layer wind (below the zero axis), for different values of the vertical velocity of shallow convection:  $w_{sc} = 0 \text{ m s}^{-1}$  (cross, dashed lines),  $w_{sc} = 0.02 \text{ m s}^{-1}$  (asterisk, dotted lines),  $w_{sc} = 0.1 \text{ m s}^{-1}$  (square, dash-dotted lines), and  $w_{sc} = 0.4 \text{ m s}^{-1}$  (circle, double-dashed lines). The solid lines display the gradient wind (above the zero axis) and the radial wind deduced from E-PI theory (below the zero axis). All values are nondimensional and for more clarity only the maximum of tangential wind is displayed since the differences between the tangential wind profiles for different  $w_{sc}$  can hardly be seen.

profile of radial wind that results from E-PI theory. E-PI theory assumes that  $v_b = v_g$ ; this allows  $u_b$  to be determined by Eq. (34). The radial wind profile is different to those of the unbalanced model. In the E-PI solution, a jump occurs at  $\tilde{r} = 1$  as a result of a discontinuous vorticity increase. A similar but less drastic radial flow deceleration can be seen in the unbalanced model. The vorticity values decrease with decreasing  $w_{sc}$  in the outer region; all are below the corresponding vorticity of gradient wind (not shown). The inflow tends to conserve angular momentum; this reduces the vorticity and enhances the inflow strength. Entrainment counteracts this tendency, thereby weakening the inflow.

### h. Modified E-PI

Now we present the results of applying the boundary layer model to the modified E-PI solution of Emanuel and Rotunno (2011). The application does not depend on the  $\beta$  parameter since the structure of the vortex in the outer region is completely determined by the assumption of a constant Richardson number in the outflow. Figure 11 displays radial profiles for the reference parameters  $Ro = 120$ ,  $C_H/C_D = 1$ , and  $\tilde{C}_D = 0.02$ . In contrast to the profiles obtained from the classical E-PI solution, the inflow is stronger and the supergradient

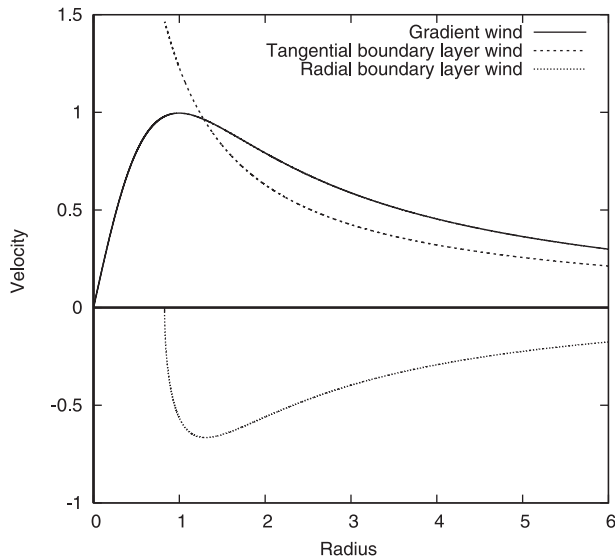


FIG. 11. As in Fig. 1, but now the gradient wind of the modified E-PI solution drives the slab boundary layer model.

winds are greater in the modified E-PI solution. Furthermore, the maximum of the gradient wind is smoother than that of the classical E-PI solution. As a consequence, the transition from small vorticity of the outer region to larger vorticity of the inner core is also smoother. We also calculated solutions for different  $C_H/C_D$  since this parameter is also important for the gradient wind outside the RMGW. Variation of  $C_H/C_D$  from 0.5 to 2.5 only leads to a slight change of maximum inflow velocity  $\tilde{u}_b$  (from 0.64 to 0.71) and maximum tangential wind  $\tilde{v}_b$  (from 1.42 to 1.47). More dramatic is the impact on the RMW, which varies between 0.684 and 1.02. Nevertheless, neither this variation nor that of other parameters yields more realistic inflow velocities. The large inflow velocity that is attained seems to be related to extremely small values of absolute gradient wind vorticity at large radii. Consequently, the modified E-PI solution leads to a more unrealistic result despite having the advantage that it does not depend on the ad hoc parameter  $\beta$ . However, we are aware that the slab boundary layer model overestimates the inflow velocity and tends to terminate the inflow too early as noted by Kepert (2010a). A more realistic outcome may appear with a less simplified boundary layer model. Figure 12 shows superintensity as a function of RMGW and Rossby number  $Ro$ . The distribution of superintensity is qualitatively similar to that shown in the lower panel of Fig. 7. However, superintensity values are more than twice as large. The RMGW of the maximum superintensity at a fixed Rossby number is also greater.

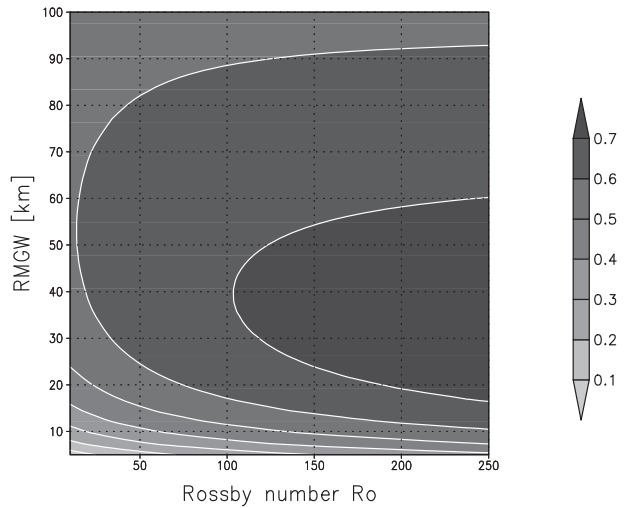


FIG. 12. As in Fig. 7 (bottom), but now the gradient wind of the modified E-PI solution drives the slab boundary layer model.

#### 4. Conclusions

The present study has extended the classical E-PI model by including gradient wind imbalance in the slab boundary model. This was made possible by the fact that the saturation entropy field in potential radius space does not depend on the gradient wind balance assumption, so long as the pressure dependence of surface entropy is neglected. We further assumed that gradient wind imbalance only occurs within the boundary layer. These assumptions lead to a model that depends upon four nondimensional parameters, namely,  $Ro = v_{g,max}/(f r_m)$ ,  $C_D r_m/H_b$ ,  $\beta$ , and  $C_H/C_D$ . The model solutions are most sensitive to  $C_D r_m/H_b$  and  $\beta$ . The drag parameter  $C_D r_m/H_b$  gives rise to a significant horizontal scale dependence of the solution. This is a novel aspect in potential intensity theory since classical E-PI theory does not depend on the RMGW of the tropical cyclone. The length scale  $H_b/C_D$  falls in the meso- $\alpha$  range of typical observed tropical cyclones. This result suggests that this length scale sets the typical diameter of a tropical cyclone. Nevertheless, the scale  $v_g/f$  could also play an important role for size control. The modified Rankine decay exponent  $\beta$  strongly influences the inflow strength in the boundary layer, with larger values of  $\beta$  leading to more intense supergradient winds. This is due to the inverse relationship between radial wind and absolute vorticity in the boundary layer. When turbulent horizontal momentum diffusion is incorporated, superintensity becomes slightly weaker and an inflow breakdown outside the RMGW does not occur. The main conclusions

from the nondiffusive model remain valid. Both the supergradient winds and the inflow velocity decrease when an entrainment effect is included in the boundary layer outside the RMGW. In the modified E-PI model of Emanuel and Rotunno (2011), the ad hoc parameter  $\beta$  becomes obsolete since the assumption of a critical outflow Richardson number enables us to extend the solution of the boundary layer entropy equation over the complete vortex. Including the unbalanced boundary layer in this model leads to very large inflow velocities and supergradient winds as a result of the low absolute vorticity outside the RMGW. The rather unrealistic result is a consequence of the low vorticity in the outer vortex. The numerical simulations by Emanuel and Rotunno reveal that the outer vortex profile is not in good agreement with that in their analytical vortex model (see their Fig. 10). They also mention that their wind model is invalid outside the radius at which the vertical velocity changes sign.

We conclude that superintensity due to supergradient winds can be described as an extension of the classical E-PI model. As a by-product we found a horizontal scale dependence of potential intensity, which is not present in E-PI based on a balanced slab boundary model. While the limitations of slab boundary models were shown by Kepert (2010a), we think that our results contribute to a qualitative understanding of supergradient winds and scale dependence of PI. Furthermore, older numerical models of tropical cyclones were often unable to resolve the boundary layer structure and may have been so coarse that the boundary layer was represented only by a single model level, which is equivalent to a slab boundary layer model. For example, Rotunno and Emanuel (1987) present results of an axisymmetric tropical cyclone model with a vertical gridpoint distance of 1.25 km. It is obvious that the boundary layer reduces to one level in such a coarse-resolution model. Kepert (2010b) presented a hybrid slab–height-parameterized boundary layer model that is more accurate. This could be coupled to the E-PI model. However, the entropy budget equation in E-PI is already based upon a slab boundary model so this approach would not be consistent. Inclusion of Kepert's improved approach to E-PI seems rather difficult. It may not be practicable to build an analytical model for PI with his boundary layer model. The conclusions drawn from this study still have to be evaluated by a more complex model. This remains a prospect for a future study.

*Acknowledgments.* This work was supported by the DFG within the Cluster of Excellence 177 Integrated Climate System Analysis and Prediction (CliSAP). We gratefully acknowledge the support of the NCAR

Advanced Study Program (ASP), the NCAR Earth Systems Laboratory, and the NCAR Research Applications Laboratory. This collaboration was also aided by ASP's Graduate Visitor Program. We thank Yuqing Wang, Kerry Emanuel, and two anonymous reviewers for their critical comments. Furthermore, we appreciate the support of Brian Tang, who read an earlier version of our manuscript and provided helpful remarks.

## APPENDIX

### Derivation of the Modified E-PI Solution

In Emanuel and Rotunno (2011) it was assumed that the outflow develops a stratification at a critical Richardson number  $Ri_c$ . Their analysis leads to the following approximate result

$$\left. \frac{\partial T_o}{\partial M} \right|_{r=r_t} = -\frac{Ri_c}{r_t^2} \frac{dM}{ds^*}, \quad (\text{A1})$$

where  $T_o$  is the outflow temperature at the outflow radius  $r = r_t$ . Since the outflow temperature is not a constant anymore, the thermal wind balance equation has to be written as follows:

$$\frac{1}{r_g^2} = -\frac{2}{f^2 R^3} (T_g - T_o) \frac{\partial s^*}{\partial R}. \quad (\text{A2})$$

Using the potential radius definition  $R = (2M/f)^{1/2}$ , we obtain

$$M_g = -r_g^2 (T_g - T_o) \frac{ds^*}{dM_g}. \quad (\text{A3})$$

Finally, we have the solution (10) of the entropy budget equation (9), which gives the saturation entropy as a function of angular momentum, namely

$$s^* = s_a^* - s_o \left( \frac{M}{M_m} \right)^{C_H/C_D}, \quad (\text{A4})$$

where  $s_o = C_H/(T_s - T_t)$  and  $M_m$  is the angular momentum whose surface intersects the RMGW at  $z = z_g$ . Inserting this result into Eqs. (A1) and (A3) leads to

$$\left. \frac{\partial T_o}{\partial M} \right|_{r=r_t} = \frac{C_D}{C_H} \frac{Ri_c}{r_t^2} \frac{M}{s_o} \left( \frac{M_m}{M} \right)^{C_H/C_D} \quad (\text{A5})$$

and

$$M_g^2 = r_g^2 (T_g - T_o) s_o \frac{C_H}{C_D} \left( \frac{M_g}{M_m} \right)^{C_H/C_D}, \quad (\text{A6})$$

respectively. Equation (A5) can be directly integrated, which gives

$$T_o = T_i + \frac{C_D/C_H}{2 - C_H/C_D} \frac{\text{Ri}_c}{r_i^2} \frac{M_m^{C_H/C_D}}{s_o} \times (M^{2-C_H/C_D} - M_m^{2-C_H/C_D}), \quad (\text{A7})$$

where  $T_i$  is the outflow temperature of the angular momentum surface having the value  $M_m$ . Since  $T_o$  in Eq. (A6) is the outflow temperature on the angular momentum surface with  $M = M_g$ , we can eliminate the temperatures  $T_o$  and  $T_i$  by substituting Eq. (A6) into Eq. (A7), which yields

$$\left( \frac{M_g}{M_m} \right)^{2-C_H/C_D} = \frac{\frac{r^2}{r_m^2} + \frac{1}{2 - C_H/C_D} \frac{\text{Ri}_c}{r_i^2} r^2}{1 + \frac{1}{2 - C_H/C_D} \frac{\text{Ri}_c}{r_i^2} r^2}. \quad (\text{A8})$$

In this equation we have replaced  $r_g$  by  $r$  since here  $M_g$  is considered as a function of physical radius  $r$ , which at  $z = z_g$  is identical to  $r_g(R)$ . This result still contains an unknown, namely the outflow radius  $r_i$ . This radius is a unique function of  $r_m$  when the requirement that  $r_m$  is equal to the RMGW is fulfilled. To determine the wind maximum, we make use of the approximation

$$v_g \approx \frac{M_g}{r}, \quad (\text{A9})$$

which should be valid at and near the RMGW. With this approximation, the wind maximum appears at

$$r_{\max} = \left( \frac{C_H}{C_D} \frac{1}{\text{Ri}_c} \right)^{1/2} r_i. \quad (\text{A10})$$

Therefore,  $r_m$  is the RMGW only if

$$r_i^2 = \frac{C_D}{C_H} \text{Ri}_c r_m^2. \quad (\text{A11})$$

Substituting this result into Eq. (A8) leads to the desired solution:

$$\left( \frac{M_g}{M_m} \right)^{2-C_H/C_D} = \frac{2(r/r_m)^2}{2 - C_H/C_D [1 - (r/r_m)^2]}. \quad (\text{A12})$$

The maximum wind speed is still unknown and has to be determined by an additional assumption. So far we have

not fixed the integration constant  $s_o$ . It is reasonable to assume that entropy attains the environmental value at the radius  $r_o$  where the tangential wind vanishes. Therefore, by Eq. (A4) we find that

$$0 = s_a^* - s_o \left( \frac{fr_o^2}{2v_{g,\max} r_m} \right)^{C_H/C_D}, \quad (\text{A13})$$

where the approximation  $M_m \approx v_{g,\max} r_m$  has been used. On the other hand, evaluating Eq. (A12) for  $r_o \gg r_m$  gives the approximate result:

$$\left( \frac{fr_o^2}{2v_{g,\max} r_m} \right)^{2-C_H/C_D} = 2 \frac{C_D}{C_H} \quad (\text{A14})$$

so that we obtain

$$s_o = \left( \frac{1}{2} \frac{C_H}{C_D} \right)^{1/(2C_D/C_H-1)} s_a^*. \quad (\text{A15})$$

By inserting the last relation in Eq. (A6) we get

$$M_g^2 = r_g^2 (T_g - T_o) \frac{C_H}{C_D} \left( \frac{1}{2} \frac{C_H}{C_D} \right)^{1/[2(C_D/C_H)-1]} s_a^* \left( \frac{M_g}{M_m} \right)^{C_H/C_D}. \quad (\text{A16})$$

Evaluation of this equation at  $r_g = r_m$  and making the approximation  $M_m \approx v_{g,\max} r_m$  leads to the desired result

$$v_{g,\max}^2 = (T_g - T_i) \frac{C_H}{C_D} \left( \frac{1}{2} \frac{C_H}{C_D} \right)^{1/[2(C_D/C_H)-1]} s_a^*, \quad (\text{A17})$$

which agrees with Eq. (28).

REFERENCES

Bryan, G. H., 2012: Effects of surface exchange coefficients and turbulence length scales on the intensity and structure of numerically simulated hurricanes. *Mon. Wea. Rev.*, **140**, 1125–1143.  
 —, and R. Rotunno, 2009: Evaluation of an analytical model for the maximum intensity of tropical cyclones. *J. Atmos. Sci.*, **66**, 3042–3060.  
 Cotton, W. R., and R. A. Anthes, 1989: *Storm and Cloud Dynamics*. Academic Press, 880 pp.  
 Emanuel, K. A., 1986: An air–sea interaction theory for tropical cyclones. Part I: Steady-state maintenance. *J. Atmos. Sci.*, **43**, 585–604.  
 —, 1989: The finite-amplitude nature of tropical cyclogenesis. *J. Atmos. Sci.*, **46**, 3431–3456.  
 —, 1995: Sensitivity of tropical cyclones to surface exchange coefficients and a revised steady-state model incorporating eye dynamics. *J. Atmos. Sci.*, **52**, 3969–3976.  
 —, 1997: Some aspects of hurricane inner-core dynamics and energetics. *J. Atmos. Sci.*, **54**, 1014–1026.

- , 2003: Tropical cyclones. *Annu. Rev. Earth Planet. Sci.*, **31**, 75–104.
- , and R. Rotunno, 2011: Self-stratification of tropical cyclone outflow. Part I: Implications for storm structure. *J. Atmos. Sci.*, **68**, 2236–2249.
- Frank, W. M., 1977: The structure and energetics of the tropical cyclone. I. Storm structure. *Mon. Wea. Rev.*, **105**, 1119–1135.
- Frisius, T., and D. Schönemann, 2012: An extended model for the potential intensity of tropical cyclones. *J. Atmos. Sci.*, **69**, 641–661.
- Hausman, S. A., K. V. Ooyama, and W. H. Schubert, 2006: Potential vorticity structure of simulated hurricanes. *J. Atmos. Sci.*, **63**, 87–108.
- Kepert, J. D., 2010a: Slab- and height-resolving models of the tropical cyclone boundary layer. Part I: Comparing the simulations. *Quart. J. Roy. Meteor. Soc.*, **136**, 1686–1699.
- , 2010b: Slab- and height-resolving models of the tropical cyclone boundary layer. Part II: Why the simulations differ. *Quart. J. Roy. Meteor. Soc.*, **136**, 1700–1711.
- Mallen, K. J., M. T. Montgomery, and B. Wang, 2005: Reexamining the near-core radial structure of the tropical cyclone primary circulation: Implications for vortex resiliency. *J. Atmos. Sci.*, **62**, 408–425.
- Persing, J., and M. T. Montgomery, 2003: Hurricane superintensity. *J. Atmos. Sci.*, **60**, 2349–2371.
- Rotunno, R., and K. A. Emanuel, 1987: An air–sea interaction theory for tropical cyclones. Part II: Evolutionary study using a nonhydrostatic axisymmetric numerical model. *J. Atmos. Sci.*, **44**, 542–561.
- , and G. H. Bryan, 2012: Effects of parameterized diffusion on simulated hurricanes. *J. Atmos. Sci.*, **69**, 2284–2299.
- Smith, R. K., 2003: A simple model of the hurricane boundary layer. *Quart. J. Roy. Meteor. Soc.*, **129**, 1007–1027.
- , M. T. Montgomery, and S. Vogl, 2008: A critique of Emanuel’s hurricane model and potential intensity theory. *Quart. J. Roy. Meteor. Soc.*, **134**, 551–561.
- Wang, Y., 2009: How do outer spiral rainbands affect tropical cyclone structure and intensity? *J. Atmos. Sci.*, **66**, 1250–1273.
- , and J. Xu, 2010: Energy production, frictional dissipation, and maximum intensity of a numerically simulated tropical cyclone. *J. Atmos. Sci.*, **67**, 97–116.
- Willoughby, H. E., 2011: The golden radius in balanced atmospheric flows. *Mon. Wea. Rev.*, **139**, 1164–1168.
- Xu, J., and Y. Wang, 2010: Sensitivity of the simulated tropical cyclone inner-core size to the initial vortex size. *Mon. Wea. Rev.*, **138**, 4135–4157.